Giuliano Allegri
Advanced Composites Centre for Innovation
and Science (ACCIS),
University of Bristol,
Bristol BS8 1TR, UK
e-mail: giuliano.allegri@bristol.ac.uk

Fabrizio Scarpa
Bristol Centre for Nanoscience and Quantum
Information (NSQI),
University of Bristol,
Bristol BS8 1TR, UK
e-mail: f.scarpa@bristol.ac.uk

Rajib Chowdhury
Department of Civil Engineering,
Indian Institute of Technology,
Roorkee 247 667, India
e-mail: Rajibfce@litr.ernet.in

Sondipon Adhikari
Multidisciplinary Nanotechnology Centre,
Swansea University,
Swansea SA2 8PP, UK
e-mail: s.adhikari@swansea.ac.uk

Wave Propagation in Periodically Supported Nanoribbons: A Nonlocal Elasticity Approach

We develop an analytical formulation describing propagating flexural waves in periodically simply supported nanoribbons by means of Eringen's nonlocal elasticity. The nonlocal length scale is identified via atomistic finite element (FE) models of graphene nanoribbons with Floquet's boundary conditions. The analytical model is calibrated through the atomistic finite element approach. This is done by matching the nondimensional frequencies predicted by the analytical nonlocal model and those obtained by the atomistic FE simulations. We show that a nanoribbon with periodically supported boundary conditions does exhibit artificial pass-stop band characteristics. Moreover, the nonlocal elasticity solution proposed in this paper captures the dispersive behavior of nanoribbons when an increasing number of flexural modes are considered. [DOI: 10.1115/1.4023953]

1 Introduction

Nonlocal elasticity [1] has the ability to bridge continuum mechanics with the deformation mechanisms existing at nanoscales, and for this reason it has been extensively used within the field of nanomechanics. Eringen's nonlocal elasticity has been applied to the mechanics of nanotubes and nanorods, with particular emphasis on describing their vibrational characteristics [2–6], and their wave propagation behavior [6,7].

For the specific case of graphene, nonlocal elasticity approaches have been employed to identify buckling loads [8,9] and to describe ultrasonic wave propagation [10,11]. Because research and development investments for the next generation of nanoelectronics [12,13] and nanoelectromechanical systems (NEMS) [14] focus on graphene, there exists a growing interest to correlate the vibration behavior of graphene nanostructures to their peculiar electronic states [15]. A typical example of a nanoelectronics device based on graphene is the 100 GHz transistor described in [16] (Fig. 1(*a*)). From the layout of the transistor, one can observe the presence of regularly spaced bridges supporting the graphene. From a structural point of view, this device can be described as a continuous beam with periodic supports. Periodic (or periodically supported) structures have been extensively studied in dynamics because of their interesting bandgap characteristics [17–19].

Graphene nanoribbons (GNRs) have attracted significant interest as potential candidates for nanoelectronics/NEMS devices [20]. GNRs have electronic states that are deeply affected by their edge structure. The zig-zag layout of the latter provides edge localized states, with nonbonding molecular orbitals close to the Fermi's energy [21]. Simulations based on density functional theory (DFT) have shown that zig-zag GNRs can exhibit either metallic or half-metallic behavior. On the other hand, armchair nanoribbons are semiconducting. The energy gaps of armchair configurations reduces for an increasing width of the GNRs [22–24]. In photonics application, GNRs have been employed as waveguides operating in

the high GHz range [25] and also to control thermal conductivity [26]. GNRs in periodically bridged configurations, as those shown in Figs. 1(*a*) and 1(*b*), have been considered for obtaining tunable bandgaps in terms of wave propagation behavior. These bandgaps are essentially dependant on the dimensions, chirality, and lengths of the GNRs [15].

Considering the wave propagation in single and multiwalled nanotubes, the nonlocal length scale considered in models usually ranges between 0.5 nm and 1 nm [27]. Smaller values have been reported for the case of rotating nanotubes [5]. In literature, the nonlocal length scale is usually denoted as $e_0 a$, where a is an internal characteristic length scale, and e_0 is an empirical constant. The latter is employed to calibrate the nonlocal models according to suitable data at atomistic level, e.g., dispersion curves. A nonlocal length scale of $e_0 a = 1$ nm has been employed to simulate the wave dispersion in single layer graphene sheets [10,11]. Interestingly, all the aforementioned nonlocal length values are well above the equilibrium distance between sp^2 C─C bonds (0.142 nm), with a resulting e_0 value of 7.04.

The wave propagation in periodically simply supported (PSS) GNRs is also affected by the additional boundary conditions that represent the supports. A legitimate question is whether the nonlocal length scale values reported in open literature are appropriate to describe the dynamic behavior of PSS-GNRs or not. In order to answer this point, we introduce an analytical expression for the dispersion curves of PSS-GNRs. This is based on the formulation originally developed by Mead [17] for "classical" (i.e., local) Euler–Bernoulli beams. We extend Mead's approach to Eringen's nonlocal elasticity. In order to identify the nonlocal length scale for PSS-GNRs, we employ an atomistic finite element (FE) framework that we previously developed and applied to single [28,29], bilayer [30,31] and hydrogenated graphene [32]. The same atomistic-FE approach has been used to identify the shear modulus of single layer graphene manufactured via chemical vapor deposition (CVD) [33]. The nonlocal length scale is obtained by matching the analytical dispersion curves with those obtained from the atomistic-FE simulations via an error minimization procedure. We show that the nonlocal length scale decreases with the number of dispersive modes considered.
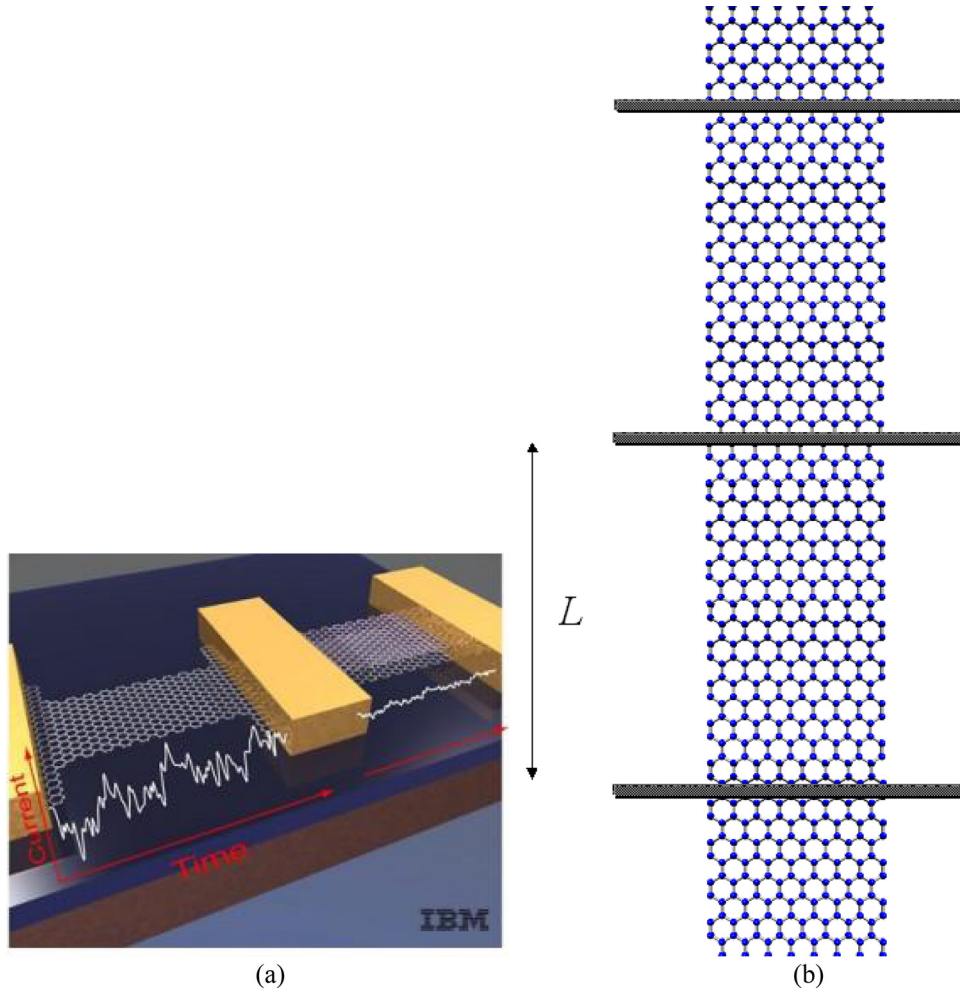
Fig. 1 (*a*) 100 GHz transistor design based on Ref. [16]. (*b*) Scheme of the periodically supported nanoribbon considered in this work.

2 Nonlocal Elasticity Formulation for Periodic Nanoribbons

2.1 Nonlocal Euler Bernoulli Beam. The equation ruling the forced vibrations of a nonlocal Euler–Bernoulli beam in bending is given as follows [8]:

$$EI\frac{\partial^4 w}{\partial x^4} + \rho A\left[\frac{\partial^2 w}{\partial t^2} - (e_0 a)^2 \frac{\partial^4 w}{\partial x^2 \partial t^2}\right] = q - (e_0 a)^2 \frac{\partial^2 q}{\partial x^2} \quad (1)$$

where w is the magnitude of the traversal displacement; ρ and E are the material density and Young's modulus, respectively; A is the beam cross-sectional area; I the beam second moment of area with respect to the longitudinal axis x; q is the distributed shear force acting in the direction normal to the x axis. Let us assume that a harmonic shear force $P_0 e^{j\omega t}$ is applied on the beam at $x = 0$. Then, from Eq. (1), it follows that the beam dynamics is governed by the following differential equation:

$$c^2 R^2 \frac{\partial^4 w}{\partial x^4} + \frac{\partial^2 w}{\partial t^2} - (e_0 a)^2 \frac{\partial^4 w}{\partial x^2 \partial t^2} = P_0\left[1 - 2\left(\frac{e_0 a}{x}\right)^2\right]\delta(x)e^{j\omega t} \quad (2)$$

where $\delta(x)$ is the Dirac's delta function, c is the speed of longitudinal elastic waves, and R is the radius of gyration of the beam cross section. The latter parameters are expressed as

$$c = \sqrt{\frac{E}{\rho}}, \quad R = \frac{h}{2\sqrt{3}} \quad (3)$$

where h is the cross-sectional height, that corresponds to the GNR thickness. In Eq. (2), we took advantage of the Dirac's delta property $x^2\delta''(x) = 2\delta(x)$. The expression of a flexural wave that satisfies Eq. (2) is

$$w(x, t) = Ae^{j\omega t + \bar{k}x} \quad (4)$$

Substituting Eq. (4) into Eq. (2), one obtains the following algebraic equation for the wave-number k for $x \neq 0$:

$$\bar{k}^4 - \frac{\omega^2}{c^2 R^2}\left[1 - (e_0 a)^2 \bar{k}^2\right] = 0 \quad (5)$$

Equation (5) governs the dispersion curves for the nonlocal beam considered here. Introducing the normalized angular frequency

$$\Omega = \frac{\omega L^2}{cR} \quad (6)$$

where L is the beam segment length, then the solution of Eq. (5) can be expressed as

$$\bar{k}_{1,2}^2 = \frac{\Omega^2}{2L^2}\left(-\lambda^2 \pm \sqrt{\lambda^4 + \frac{4}{\Omega^2}}\right) \quad (7)$$

where

$$\lambda = \frac{e_0 a}{L} \tag{8}$$

Equation (7) possesses two real and two complex conjugate roots. In the limit $\lambda \to 0$, the expressions of the wave-numbers become those given in classical elastodynamics [17]. Equations (4) and (7) imply the existence of the following two flexural waves in nonlocal dynamics:

$$
\begin{aligned}
w_1(x,t) &= \left(A_1 e^{-\bar{k}_1 x} + A_2 e^{-\bar{k}_2 x} \right) e^{j\omega t}, \quad x \geq 0, \\
w_2(x,t) &= \left(A_1 e^{\bar{k}_1 x} + A_2 e^{\bar{k}_2 x} \right) e^{j\omega t}, \quad x \leq 0
\end{aligned} \tag{9}
$$

The first of Eqs. (9) represents the wave traveling towards the right of the harmonic force application point. Similarly, the second of Eqs. (9) gives the left-traveling flexural wave with respect to the point where the harmonic load acts.

2.2 Simply Supported Periodical Euler–Bernoulli Beam. We now assume that the nonlocal Euler–Bernoulli beam is periodic with characteristic length L. Let the beam be simply supported at the center of each periodic segments, i.e., at $x = 0$ in the present case. As a consequence, a harmonic reaction force $P_0 e^{j\omega t}$ is applied at $x = 0$. Due to the antisymmetry conditions holding at the point of application of the reaction force, one obtains

$$\left. \frac{\partial w_1}{\partial x} \right|_{x=0} = \left. \frac{\partial w_2}{\partial x} \right|_{x=0} = 0 \tag{10}$$

Applying the boundary conditions from Eq. (10) to Eq. (9) leads to the following expression:

$$A_2 = -\frac{\bar{k}_1}{\bar{k}_2} A_1 \tag{11}$$

The shear resultant for a nonlocal Euler–Bernoulli beam is expressed as

$$Q = -EI \frac{\partial w^3}{\partial x^3} + (e_0 a)^2 \left(\rho A \frac{\partial^3 w}{\partial x \partial^2 t} - \frac{\partial q}{\partial x} \right) \tag{12}$$

For $x \to 0^+$, the shear resultant at the support is given by

$$Q = \frac{P_0}{2} e^{j\omega t} \tag{13}$$

In order to obtain a further relation for the constant A_1 and A_2, one has to substitute the general expression of the displacement $w_1(x,t)$ from the first of Eqs. (9) into Eq. (12) and impose the natural boundary condition from Eq. (13). It is worth observing that in Eq. (12)

$$\lim_{x \to 0+} \frac{\partial q}{\partial x} = \lim_{x \to 0+} P_0 \frac{\partial \delta(x)}{\partial x} e^{j\omega t} = -\lim_{x \to 0+} P_0 \frac{\delta(x)}{x} e^{j\omega t} = 0 \tag{14}$$

Therefore, proceeding as outlined above, the following equation is sought:

$$\frac{P_0}{2} = EI \left(\bar{k}_1^3 A_1 + \bar{k}_2^3 A_2 \right) + (e_0 a)^2 \rho A \omega^2 \left(\bar{k}_1 A_1 + \bar{k}_2 A_2 \right) \tag{15}$$

Solving the linear system of Eqs. (11) and (15) with respect to A_1 and A_2 yields

$$A_1 = \frac{P_0}{2EI\bar{k}_1(\bar{k}_1^2 - \bar{k}_2^2)}, \quad A_2 = -\frac{P_0}{2EI\bar{k}_2(\bar{k}_1^2 - \bar{k}_2^2)} \tag{16}$$

Alternatively, the same expressions of A_1 and A_2 can be obtained by considering the limit $x \to 0^-$. In the latter case, however, the natural boundary condition reads as $Q = -(P_0/2)e^{j\omega t}$ and the displacement $w_2(x,t)$ from the second of Eqs. (9) must be considered. Substituting Eqs. (16) into the first of Eqs. (9) leads to

$$w_1(x,t) = \frac{P_0}{2EI} \left[\frac{1}{\bar{k}_1(\bar{k}_1^2 - \bar{k}_2^2)} e^{-\bar{k}_1 x} - \frac{1}{\bar{k}_2(\bar{k}_1^2 - \bar{k}_2^2)} e^{-\bar{k}_2 x} \right] e^{j\omega t} \tag{17}$$

As a consequence, the displacement at the support point, i.e., for $x = 0$, can be rearranged as

$$w_1(0,t) = P_0 \sum_{n=1}^{2} a_n e^{j\omega t} \tag{18}$$

where

$$
\begin{cases}
a_1 = \dfrac{1}{2EI} \dfrac{1}{\bar{k}_1(\bar{k}_1^2 - \bar{k}_2^2)} \\[2ex]
a_2 = \dfrac{1}{2EI} \dfrac{1}{\bar{k}_2(\bar{k}_2^2 - \bar{k}_1^2)}
\end{cases} \tag{19}
$$

As demonstrated by Mead [34], for a phased array of support forces $P_r = P_0 e^{\mu r + j\omega t}$ acting on the periodic beam with spatial period L, the total displacement at the support points is given by

$$w_{0P} = P_0 \sum_{n=1}^{2} a_n \frac{\sinh \bar{k}_n L}{\cosh \bar{k}_n L - \cosh \mu} \tag{20}$$

where μ is the attenuation constant representing the dispersion properties of the periodic beam. The latter can be easily determined by observing that at every support location the displacement given in Eq. (20) must be zero. Thus, solving Eq. (20) with respect to μ for $w_{0P} = 0$ yields

$$\cosh \mu = \frac{\bar{k}_2 \cosh \bar{k}_2 L \sinh \bar{k}_1 L - \bar{k}_1 \cosh \bar{k}_1 L \sinh \bar{k}_2 L}{\bar{k}_2 \sinh \bar{k}_1 L - \bar{k}_1 \sinh \bar{k}_2 L} \tag{21}$$

The propagation constant k associated with the PSS-GNR configuration is the imaginary part of the attenuation constant

$$k = \mathrm{Im}(\mu) \tag{22}$$

In the limit $\lambda \to 0$, i.e., for a "classical" Euler–Bernoulli beam, Eq. (7) yields the following wave-numbers:

$$\bar{k}_1 = \pm j\bar{k}, \quad \bar{k}_2 = \pm \bar{k}, \quad \bar{k} = \sqrt{\frac{\omega}{cR}} \tag{23}$$

Note that for $z \in \mathbb{R}$, $\sinh jz = j \sin z$, and $\cosh jz = \cos z$. Thus, in the limit $\lambda \to 0$, Eq. (21) becomes

$$\cosh \mu = \frac{\cosh \bar{k}L \sin \bar{k}L - \cos \bar{k}L \sinh \bar{k}L}{\sin \bar{k}L - \sinh \bar{k}L} \tag{24}$$

The relation (24) is the well-known expression of the attenuation constant for PSS Euler–Bernoulli beams derived from classical elasticity [17,34].

3 Atomistic-FE Model

We employ an atomistic-continuum equivalence model for the sp^2 carbon-carbon bonds to extract the equivalent isotropic mechanical properties (Young's modulus and Poisson's ratio) as functions of the thickness d of the C—C bond. It is worth stressing that the atomistic-FE model is based on classical, i.e., local,

elasticity. We aim to establish under which conditions the nonlocal analytical model is able to match the dispersion curves generated by the atomistic-FE simulations.

The atomistic-FE model is based on the equivalence between the harmonic potential provided by force models, such as AMBER or linearized Morse, and the strain energies associated to axial, bending, and out-of-plane torsional deformations of a deep shear Timoshenko beam [15]

$$
\begin{cases}
\dfrac{k_r}{2}(\Delta r)^2 = \dfrac{E_Y A}{2a}(\Delta r)^2 \\[2mm]
\dfrac{k_\tau}{2}(\Delta\varphi)^2 = \dfrac{GJ}{2a}(\Delta\varphi)^2 \\[2mm]
\dfrac{k_\theta}{2}(\Delta\theta)^2 = \dfrac{E_Y I}{2a}\dfrac{4+\Phi}{1+\Phi}(\Delta\theta)^2
\end{cases}
\tag{25}
$$

The first of Eqs. (25) represents the energetic equivalence between the C—C bond stretching and the beam axial deformation. E_Y is the equivalent Young's modulus. The second of Eqs. (25) relates the torsional deformation of the C—C bond with the twisting of a beam whose shear modulus is G. In the third of Eqs. (25), the term related to the in-plane rotation of the C—C bond is equated to the bending strain energy associated with a deep shear beam model. This approach differs from other models presented in the literature since it accounts for the shear deformation of the beam cross section. The shear correction term becomes necessary when beams assume aspect ratios lower than 10, which is indeed the case for the C—C bonds according to the open literature [35]. For circular cross sections, the shear deformation constant can be expressed as [15]

$$
\Phi = \frac{12EI}{GA_s a^2}
\tag{26}
$$

In Eq. (26), $A_s = A/F_s$ is the reduced cross section of the beam, where F_s is the shear correction term. The latter is given by

$$
F_s = \frac{6 + 12\nu + 6\nu^2}{7 + 12\nu + 4\nu^2}
\tag{27}
$$

Inserting Eqs. (26) and (27) into Eq. (25) leads to an nonlinear relation between the thickness d and the Poisson's ratio ν of the equivalent beam

$$
k_\theta = \frac{k_r d^2}{16}\frac{4A+B}{A+B}
\tag{28}
$$

where

$$
A = 112a^2 k_\tau + 192a^2 k_\tau \nu + 64a^2 k_\tau \nu^2
\tag{29}
$$

$$
B = 9k_r d^2 + 18k_r d^4 \nu + 9k_r d^4 \nu^2
\tag{30}
$$

The values for the force constants for the linearized Morse potential model are $k_r = 8.74 \times 10^{-7}\,\mathrm{N\,mm^{-1}}$, $k_\theta = 9.00 \times 10^{-10}\,\mathrm{N\,nm\,rad^{-2}}$, and $k_\tau = 2.78 \times 10^{-10}\,\mathrm{N\,nm^{-1}\,rad^{-2}}$. The equivalent mechanical properties of the C—C bond are determined from Eqs. (25) via a nonlinear optimization based on the Marquardt's algorithm. When using the linearized Morse potential, the value of the bond thickness d is 0.074 nm [28]. The same value was identified by Zhou et al. [36] in single and multiwalled carbon nanotubes. Huang et al. [37] have obtained a bond thickness of 0.056 nm for single layer graphene sheets represented by first and second order Tersoff–Brenner potentials and subjected to in-plane loading. Following the identification of the equivalent elastic constants, each C—C bond is discretized as a three-dimensional beam finite element bounded by two nodes. Each node has six degrees of freedom (DOFs). The C atoms are located at the nodes. The beam stiffness matrix $[\mathbf{K}]_\mathbf{e}$ is given in Ref. [38]. The elemental mass matrix $[\mathbf{M}]_\mathbf{e}$

is derived assuming that the atom masses are lumped at the nodes. Its expression is given in Ref. [15]. The mass of the C atom is $m_c = 1.9943 \times 10^{-26}\,\mathrm{kg}$. The elemental matrices are then assembled in the usual FE fashion into global stiffness and mass matrices $[\mathbf{K}]$ and $[\mathbf{M}]$, respectively.

The 1D wave propagation analysis is carried out using the technique implemented in Ref. [39]. Applying the Floquet's conditions between the left and right nodal DOFs $\{\mathbf{u}\}^L$ and $\{\mathbf{u}\}^R$ one obtains

$$
\{\mathbf{u}\}^L = e^{-ik}\{\mathbf{u}\}^R
\tag{31}
$$

where $-\pi \leq k \leq \pi$ is the propagation constant within the first Brillouin zone. The generalized DOFs of the system will be complex (real and imaginary part), while for traveling waves the propagation constant k will be solely real [40]. Therefore, Eqs. (31) can be recast as

$$
\begin{aligned}
\{\mathbf{u}\}_{\mathrm{Im}}^L &= \{\mathbf{u}\}_{\mathrm{Im}}^R \cos k - \{\mathbf{u}\}_{\mathrm{Re}}^R \sin k \\
\{\mathbf{u}\}_{\mathrm{Re}}^L &= \{\mathbf{u}\}_{\mathrm{Im}}^R \cos k + \{\mathbf{u}\}_{\mathrm{Re}}^R \sin k
\end{aligned}
\tag{32}
$$

The PSS-GNR nanoribbon model has developed following the method outlined in Ref. [15]. The real and imaginary parts of the solution domain are simulated in the FE model by creating two superimposed meshes that are linked by the boundary conditions in Eq. (32). For a given wave propagation constant k, the resultant eigenvalue problem provides the frequency associated with the wave dispersion curve. Inessential rigid motions are prevented by constraining the nodes at one end of the PSS-GNR model.

## 4 Numerical Optimization Procedure

The attenuation constants given in Eqs. (21) can be evaluated for a prescribed range of normalized frequencies Ω at a given nonlocal distance. Thus, the propagation constant k from Eq. (22) is a function of both the frequency and the nonlocal distance $e_0 a$. For each value of the GNR length and width, the nonlocal distance is identified by means of an optimization routine, where the following cost function is minimized with respect to $e_0 a$:

$$
C(e_0 a) = \sqrt{\sum_{p=1}^{M}\sum_{m=1}^{N_p}\left[1 - \frac{\Omega_m^{(p)}(e_0 a)}{\hat{\Omega}_m^{(p)}(e_0 a)}\right]^2}
\tag{33}
$$

where $\hat{\Omega}_m^{(p)}$ is the normalized frequency obtained from the atomistic-FE simulations at the wavenumber k_m for the pth mode; $\Omega_m^{(p)}$ is the normalized frequency yielded from the nonlocal analytical model presented here, again evaluated at k_m for the pth mode. In Eq. (33), N_p represents the total number of data points obtained from the finite element simulations for the pth. However, k is the independent variable in the atomistic-FE simulations, while the normalized frequency is the independent variable in the analytical model Eq. (21). Therefore, in order to evaluate the frequencies at the same set of wave-numbers k_m in Eq. (33), the analytical solution is approximated by a piecewise cubic spline interpolation within the optimization routine. The mean square error associated with this approximation was below 0.1% for the all test cases considered here. The optimization algorithm is based on a simple golden section search, coupled with parabolic interpolation. This is adequate for the minimization problem considered in this work, since the function $C(e_0 a)$ is defined in a bounded interval and relatively smooth.

5 Results and Discussions

We here assume that the internal characteristic length scale a equals the equilibrium length of the C—C bonds, i.e., $a = 0.142$ nm. Consequently, we adjust the value of the empirical
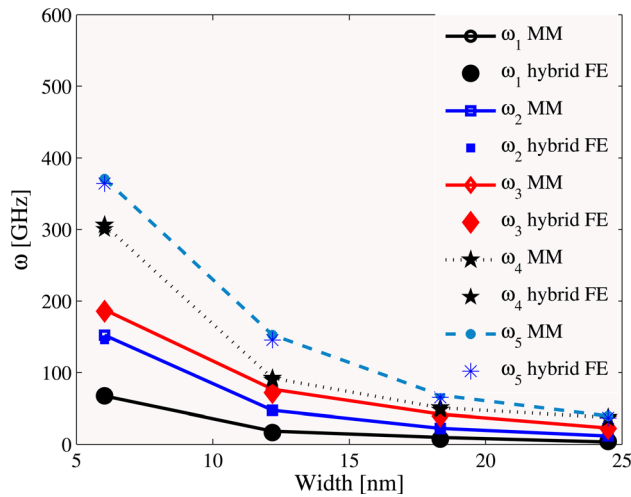
Fig. 2 Comparison between predicted natural frequencies for (8,0) nanoribbons at different length when considering the atomistic-FE approach and molecular mechanics models (from Ref. [15])

constant e_0 in order to match the analytical dispersion curves with those generated by the atomistic-FE simulations. We will denote e_0 as the ''nonlocality parameter'' from now on.

The reference GNR configuration used in this work (i.e., that corresponding to the local elasticity solution) is represented by a (8,0) graphene sheet with dimensions $L = 17.11$ nm, $B = 2.282$ nm (1780 atoms) (Fig. 2). For this reference configuration one has $L/a = 120$. Figure 3 shows the first six free-free modes of the GNR. The natural frequencies range from 4.24 GHz to 152.34 GHz. All the modes are beamlike flexural, with the first torsional mode arising after the 6th bending one (the torsional mode is not shown in Fig. 3).

The density of the continuum material representing the GNR has been computed from the total mass of the nanostructural FE model, divided by the volume of the GNR itself. This gives a density value of 2430 kgm^{-3}.

The equivalent flexural modulus of the GNR was extracted from the analytical expressions of the first four natural frequencies [41], providing a Young's modulus of 4.77 TPa. Huang et al. [37] reported an in-plane Young's modulus on 4.27 TPa when using second generation Tersoff–Brenner potentials to simulate uniaxial stretching of graphene. If we consider the tensile rigidity $Y = Ed$ of the nanostructure as a metrics for comparison, our predicted value is 0.353 TPa nm. This is well in agreement with the value of 0.363 TPa nm identified by Yakobson et al. [42], the 0.360 TPa nm obtained by Chang and Gao [43], and finally the 0.348 TPa nm reported by Tu and Ou-Yang [44]. It is also worth noticing that the experimental value for the in-plane tensile rigidity of graphite is 0.342 TPa nm [45], while the analogous value measured through AFM indentation on single layer graphene sheets is 0.335 TPa nm [46]. The tensile rigidity value of 0.353 TPa nm identified in this work has been then used to calculate the analytical dispersion curves Eq. (21) by means of the nonlinear minimization procedure based on the cost function in Eq. (33).

The dispersion curves for to the reference (8,0) GNR are shown in Fig. 4. It is possible to observe clear band-gaps between 11 GHz and 19 GHz, 36 GHz and 29 GHz, 57 GHz and 72 GHz, 92 GHz and 110 GHz, and finally 134 GHz and 160 GHz. The operating mode shapes for the first five dispersion branches are all flexural. The associated mode shapes of the reference (8,0) GNR are those shown in Fig. 5 for $k = \pi$. It is possible to observe mode veering between torsional and flexural waves within the 6th and 7th dispersion branches. This effect is particularly evident for $0.7 < k/\pi < 0.8$. For $k/\pi > 0.8$, the 6th dispersive branch is actually associated with a propagating fully torsional mode. Regarding the first five dispersive modes, the reference GNR
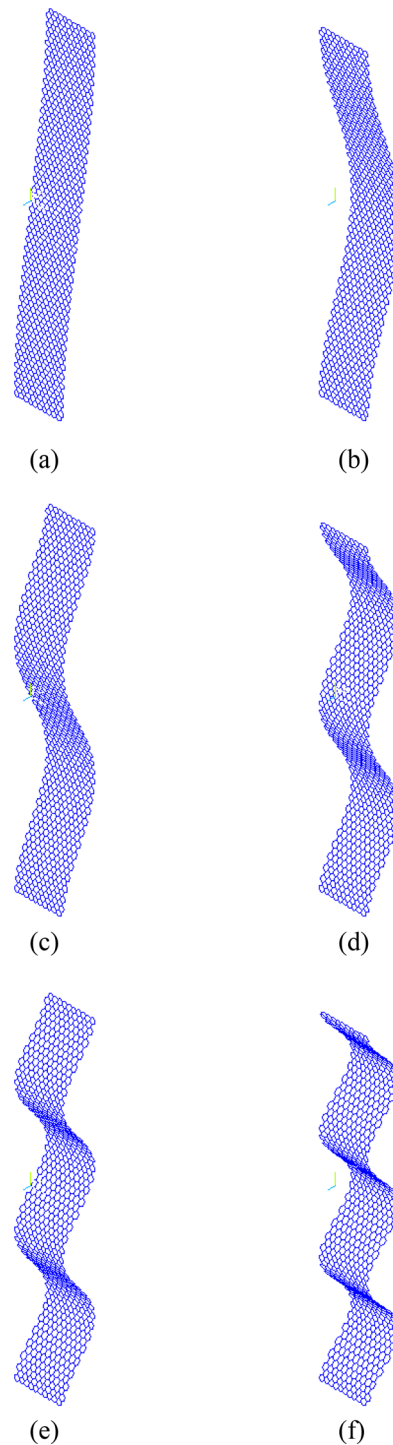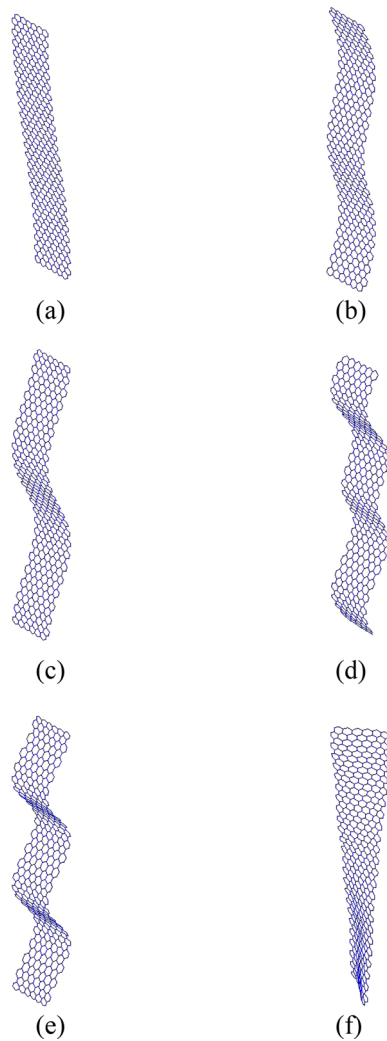

Fig. 3 First six mode shapes of a (8,0) nanoribbon with 1780 atoms. (a) 4.24 GHz, (b) 16.90 GHz, (c) 38.15 GHz, (d) 67.80 GHz, (e) 105.87 GHz, and (f) 152.34 GHz.

considered in this work behaves for as a Euler–Bernoulli beam, following the dispersive behavior of the PSS beams described by Mead [17,34].

Figure 6 shows the first dispersion curve Ω_1 versus the propagation constant for different nonlocality parameters e_0. The overall trend of the dispersion curves is not affected by the magnitude of the nonlocal length scale. The nondimensional frequencies Ω have higher values for $k \to 0$ and decrease monotonically for $k \to \pi$. An increasing e_0 decreases the overall magnitude of the dispersion curve. The frequency drops by approximately 30% for extremely large values of the nonlocal length scale ($e_0 = 20$).
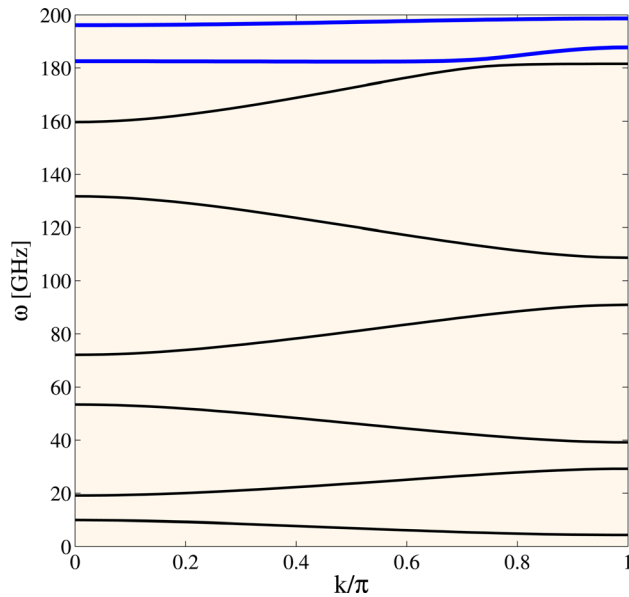
Fig. 4 Dispersion curve for the (8,0) periodically supported nanoribbon with 1780 atoms. The darker lines represent flexural modes; the lighter ones are related to torsional modes.

Fig. 5 Actual mode shapes of the first six nondimensional frequencies Ω for the reference (8,0) nanoribbon with 1780 atoms. Case $k = \pi$. (*a*) Ω_1, (*b*) Ω_2, (*c*) Ω_3, (*d*) Ω_5, (*e*) Ω_5, (*f*) Ω_6.
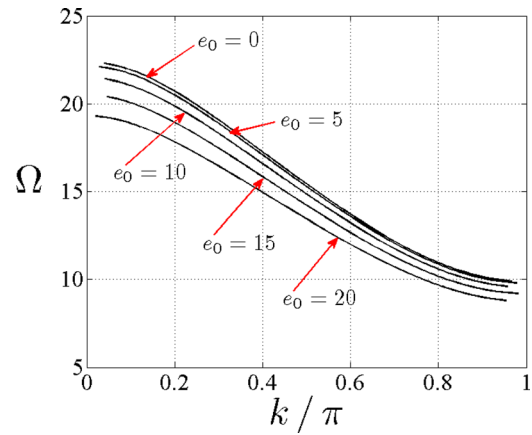

Fig. 6 Effect of the nonlocality parameter e_0 on the first dispersion curve

The variation of the first five dispersion branches obtained from the atomistic-FE simulations is presented in Fig. 7 with respect to the different dimensions of the GNRs. The same figure also shows the dispersion trends identified via the nonlocal analytical model by minimizing the cost function in Eq. (33). The model matching procedure is carried out on the first five modes. The GNR aspect ratio L/B varies from 7.80 (25.631 nm × 3.281 nm) to 5.66 (3.479 nm × 0.615 nm). The analytical nonlocal solution follows very closely the atomistic-FE model in almost all cases, except for the shortest GNR considered (Fig. 7(*i*)). In this case, the nonlocal solution underestimates by 10% the results from the atomistic-FE model. Moreover, the first torsional dispersion curve occurs before the appearance of the fifth flexural mode. This is a feature that the nonlocal model cannot capture, since only the flexural behavior is accounted for in Eq. (21). Nonetheless, for all the cases considered, the ratio L/R between the GNR length and its radius of gyration varies between 205 and 1627. This range of slenderness is well within the limits of the local model originally developed by Mead [17] and based on the Euler–Bernoulli beam theory.

The values of the nonlocality parameter e_0 identified via the nonlinear matching procedure are affected by the number of modes considered (Table 1).

Matching dispersion curves for the first mode only yields e_0 values that range from 4 to 9.8 for $24.5 < L/a < 181$. In slender nanostructures like single wall carbon nanotubes (SWCNTs) and multiwall carbon nanotubes (MWCNTs), Narendar and Gopalakrishnan have reported e_0a values varying between 0.5 nm and 2 nm, corresponding to $3.5 < e_0 < 14.1$ [26]. The situation changes significantly if more modes are used to match the atomistic-FE simulations. For both $24.5 < L/a < 110$ and $145 < L/a < 181$, the nonlocality parameter value plateaus between about 3 and 1.55 when three modes are considered. If five dispersive curves are taken into account, then the nonlocality parameters averages at about 2.0 across the various L/a values. This corresponds to at nonlocal distance of $e_0a = 0.28$ nm, higher than the 0.18 nm identified by Arash et al. in single layer square graphene sheets (15 nm × 15 nm) with fixed edges [10]. However, the nanoribbons shown in this work have shorter width, and edges effects with Floquet boundary conditions are present in our case, a situation not occurring in other papers present in open literature. The particular boundary conditions, size effects, and chirality of the nanostructure affects the nonlocal distance, as it has been demonstrated with for flexural and torsional waves in CNTs with different chirality in Ref. [47]. The optimal identification of the nonlocal parameters for a nanostructure with a given chirality and dimensions is performed using displacement time histories [10,47]. In our case, we effectively use a modal superposition technique based on the flexural waves belonging to the dispersion curves of the periodic nanoribbon, and truncation errors can arise if sufficient numbers of wavemodes are not taken into account.
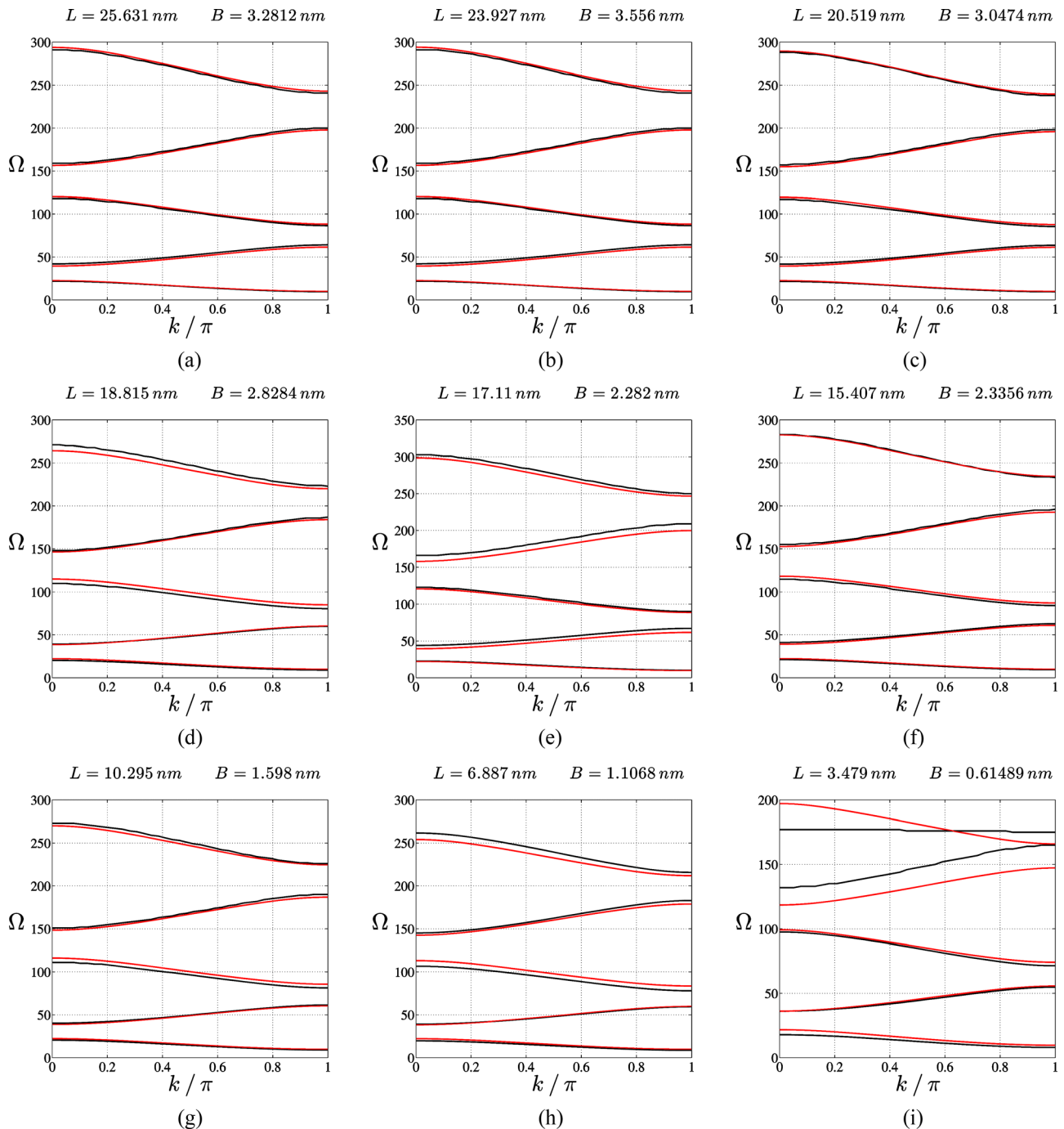
Fig. 7 Atomistic-FE results (dark lines) and analytical nonlocal model (light lines) for different lengths L of the periodic simply supported nanoribbon. Five modes used for the identification on the nonlocal parameter e_0.

Table 1 Parameter e_0 identified through least squares minimization based on the number of wave modes and L/a ratios of the nanoribbons

	First mode	First three modes	First five modes
L/a	e_0	e_0	e_0
24.5	4.33	2.01	1.72
48.5	7.41	3.68	1.84
72.5	8.66	3.01	2.10
109	9.83	3.08	2.27
145	10.1	2.76	2.25
169	9.04	1.26	1.81
181	9.83	1.55	1.99

6 Conclusions

The comparison of the analytical and atomistic-FE models in terms of wave propagation behavior of periodically simply supported nanoribbons leads to the following conclusions:

(1) For nonlocal length scales above zero, the magnitude of the nondimensional dispersion curves decreases. This drop can reach 30% for extremely high nonlocality parameters ($e_0 = 20$) with respect to the solution obtained from classical elasticity.

(2) The nonlocality parameter tends to 2.0 when an increasing number of modes is considered (up to five in this work). More modes could be taken into account. However, care has to be taken to select only flexural wavemodes when

using the nonlocal periodic Euler–Bernoulli beam model. Atomistic-FE representations of the nanoribbons would also capture propagating torsional waves, which are not included in the analytical model presented here.

Using a periodic support topology for the nanoribbons would facilitate the creation of artificial stop-pass bands in the S-band regime and also at higher bandwidths. Therefore, there is scope for extending the use of these nanostructures to the development of novel photonics devices.

References

[1] Eringen, A. C., 1983, "On Differential-Equations of Nonlocal Elasticity and Solutions of Screw Dislocation and Surface Waves," J. Appl. Phys., **54**(9), pp. 4703–4710.
[2] Li, C., Lim, C. W., Yu, J. L., and Zeng, Q. C., 2011, "Analytical Solutions for Vibration of Simply Supported Nonlocal Nanobeams With an Axial Force," Int. J. Struct. Stab. Dyn., **11**(2), pp. 257–271.
[3] Pin Lu H., Lee, P., Lu, C., and Zhang, P. Q., 2007, "Application of Nonlocal Beam Models for Carbon Nanotubes," Int. J. Solid. Struct., **44**(16), pp. 5289–5300.
[4] Narendar, S., and Gopalakrishnan, S., 2010, "Nonlocal Scale Effects on Ultrasonic Wave Characteristics Nanorods," Physica E, **42**(5), pp. 1601–1604.
[5] Narendar, S., and Gopalakrishnan, S., 2011, "Nonlocal Wave Propagation in Rotating Nanotube," Result. Phys., **1**(1), pp. 17–25.
[6] Wang, Q., 2005, "Wave Propagation in Carbon Nanotubes via Nonlocal Continuum Mechanics," J. Appl. Phys., **98**(12), p. 124301.
[7] Wang, L., and Hu, H., 2005, "Flexural Wave Propagation in Single-Walled Carbon Nanotubes," Phys Rev B, **71**, p. 195412.
[8] Pradhan, S. C., 2009, "Buckling of Single Layer Graphene Sheet Based on Nonlocal Elasticity and Higher Order Shear Deformation Theory," Phys. Lett. A., **373**(45), pp. 4182–4188.
[9] Samaei, A. T., Abbasion, S., and Mirsayar, M. M., 2011, "Buckling Analysis of a Single-Layer Graphene Sheet Embedded in an Elastic Medium Based on Nonlocal Mindlin Plate Theory," Mech. Res. Commun., **38**(7), pp. 481–485.
[10] Arash, B., Wang, Q., and Liew, K. M., 2012, "Wave Propagation in Graphene Sheets With Nonlocal Elastic Theory via Finite Element Formulation," Comput. Meth. Appl. M., **223–224**, pp. 1–9.
[11] Narendar, S., Roy Mahapatra, D., and Gopalakrishnan, S., 2010, "Investigation of the Effect of Nonlocal Scale on Ultrasonic Wave Dispersion Characteristics of a Monolayer Graphene," Comput. Mater. Sci., **49**(4), pp. 734–742.
[12] Kim, K. S., Zhao, Y., Jang, H., Lee, S. Y., Kim, J. M., Kim, K. S., Ahn, J.-H., Kim, P., Choi, J.-Y., and Hong, B. H., 2009, "Large-Scale Pattern Growth of Graphene Films for Stretchable Transparent Electrodes," Nature, **457**(7230), pp. 706–710.
[13] Zhang, Y. B., Tan, Y. W., Stormer, H. L., and Kim, P., 2005, "Experimental Observation of the Quantum Hall Effect and Berry's Phase in Graphene," Nature, **438**(7065), pp. 201–204.
[14] Sakhaee-Pour, A., Ahmadian, M. T., and Vafai, A., 2008, "Potential Application of Single-Layered Graphene Sheet as Strain Sensor," Solid State Comm., **147**(7–8), pp. 336–340.
[15] Scarpa, F., Chowdhury, R., Kam, K., Adhikari, S., and Ruzzene, M., 2011, "Dynamics of Mechanical Waves in Periodic Graphene Nanoribbon Assemblies," Nanosc. Res. Lett., **6**, pp. 430–439.
[16] Lin, Y.-M., Dimitrakopoulos, C., Jenkins, K. A., Farmer, D. B., Chiu, H.-Y., Grill, A., and Avouris, P. H., 2010, "100-GHz Transistors From Wafer-Scale Epitaxial Graphene," Science, **327**(5966), p. 662.
[17] Mead, D. J., 1970, "Free Wave Propagation in Periodically Supported, Infinite Beams," J. Sound Vib., **11**(2), pp.181–197.
[18] Mead, D. J., 1996, "Wave Propagation in Continuous Periodic Structures: Research Contributions From Southampton 1964–1995," J. Sound Vib., **190**(3), p. 495.
[19] Ruzzene, M., and Baz, A., 2000, "Attenuation and Localization of Wave Propagation in Periodic Rods Using Shape Memory Inserts," Smart Mater. Struct., **9**, p. 805.
[20] Nakada, K., Fujita, M., Dresselhaus, G., and Dresselhaus, M. S., 1996, "Edge State in Graphene Nanoribbons: Nanometer Size Effect and Edge Shape Dependence," Phys. Rev. B, **54**(24), p. 17954.
[21] Wen, J. G., Lao, J. Y., Wang, D. Z., Kyaw, T. M., Foo, Y. L., and Ren, Z. F., 2003, "Self-Assembly of Semiconducting Oxide Nanowires, Nanorods, and Nanoribbons," Chem. Phys. Lett., **372**, pp. 717–722.
[22] Barone, V., Hod, O., and Scuseria, G. V., 2006, "Electronic Structure and Stability of Semiconducting Graphene Nanoribbons," Nano. Lett., **6**(12), p. 2748.
[23] Han, M. Y., Özyilmaz, B., Zhang, Y., and Kim, P., 2007, "Energy Band-Gap Engineering of Graphene Nanoribbons," Phys. Rev. Lett., **98**(20), p. 206805.
[24] Hod, O., and Scuseria, G. E., 2009, "Electromechanical Properties of Suspended Graphene Nanoribbons," Nano Lett., **9**(7), pp. 2619–2622.
[25] Law, M., Sirbuly, D. J., Johnson, J. C., Goldberger, J., Saykally, R. J., and Yang, P., 2004, "Nanoribbon Waveguides for Subwavelength Photonics Integration," Science, **305**(5688), p. 269.
[26] Yosevich, Y. A., and Savin, A. V., 2009, "Reduction of Phonon Thermal Conductivity in Nanowires and Nanoribbons With Dynamically Rough Surfaces and Edges," Eur. Phys. Lett., **88**, p. 14002.
[27] Narendar, S., and Gopalakrishnan, S., 2009, "Nonlocal Scale Effects on Wave Propagation in Multi-Walled Carbon Nanotubes," Comput. Mater. Sci., **47**(2), pp. 526–538.
[28] Scarpa, F., Adhikari, S., and Phani, A. S., 2009, "Effective Elastic Mechanical Properties of Single Layer Graphene Sheets," Nanotechnology, **20**, p. 065709.
[29] Scarpa, F., Adhikari, S., Gil, A. J., and Remillat, C., 2010, "The Bending of Single Layer Graphene Sheets: Lattice Versus Continuum Approach," Nanotechnology, **21**(12), p. 125702.
[30] Chandra, Y., Chowdhury, R., Scarpa, F., and Adhikaricor, S., 2011, "Vibrational Characteristics of Bilayer Graphene Sheets," Thin Solid Films **519**(18), pp. 6026–6032.
[31] Scarpa, F., Adhikari, S., and Chowdhury, R., 2010, "The Transverse Elasticity of Bilayer Graphene," Phys. Lett. A, **374**, pp. 2053–2057.
[32] Scarpa, F., Chowdhury, R., and Adhikari, S., 2011, "Thickness and In-Plane Elasticity of Graphane," Phys. Lett. A, **375**(20), pp. 2071–2074.
[33] Liu, X., Metcalf, T. H., Robinson, J. T., Houston, B. H., and Scarpa, F., 2012, "Shear Modulus of Monolayer Graphene Prepared by Chemical Vapor Deposition," Nano Lett., **12**(2), pp. 1013–1017.
[34] Mead, D. J., 1986, "A New Method of Analyzing Wave Propagation in Periodic Structures; Applications to Periodic Timoshenko Beams and Stiffened Plates," J. Sound Vib., **104**(1), pp. 9–27.
[35] Huang, Y., Wu, J., and Hwang, K. C., 2006, "Thickness of Graphene and Single Wall Carbon Nanotubes," Phys Rev B, **74**, p. 245413.
[36] Xin, Z., Jianjun, Z., and Zhong-can, O.-Y., 2000, "Strain Energy and Young's Modulus of Single-Wall Carbon Nanotubes Calculated From Electronic Energy-Band Theory," Phys. Rev. B, **62**, pp. 13692–13696.
[37] Huang, Y., Wu, J., and Hwang, K. C., 2006, "Thickness of Graphene and Single-Wall Carbon Nanotubes," Phys. Rev. B, **74**, p. 245413.
[38] Przemienicki, J. S., 1968, Theory of Matrix Structural Analysis, McGraw-Hill, New York.
[39] Tee, K. F., Spadoni, A., Scarpa, F., and Ruzzene, M., 2010, "Wave Propagation in Auxetic Tetrachiral Honeycombs," ASME J. Vib. Acoust., **132**(3), p. 031007.
[40] Brillouin, L. 1953, Wave Propagation in Periodic Structures, Dover Phoenix Editions, New York.
[41] Berdichevsky, V. L., 2009, "Theory of Elastic Plates and Shells," Variational Principles of Continuum Mechanics II: Applications, Interaction of Mechanics and Mathematics, Springer, Berlin.
[42] Yakobson, B. I., Brabec, C. J., and Bernholc, J., 1996, "Nanomechanics of Carbon Tubes: Instabilities Beyond Linear Response," Phys. Rev. Lett., **76**, pp. 2511–2514.
[43] Chang, T., and Gao, H., 2003, "Size-Dependent Elastic Properties of a Single Walled Carbon Nanotube via a Molecular Mechanics Model," J. Mech. Phys. Solids, **51**, p. 1059.
[44] Tu, Z., and Ou-Yang, Z., 2002, "Single-Walled and Multiwalled Carbon Nanotubes Viewed as Elastic Tubes With the Effective Young's Moduli Dependent on Layer Number," Phys. Rev. B, **65**, p. 233407.
[45] Blakslee, O. L., Proctor, D. G., Seldin, E. J., Spence, G. B., and Weng, T., 1970, "Elastic Constants of Compression-Annealed Pyrolytic Graphite," J. Appl. Phys., **41**(8), pp. 3373–3382.
[46] Lee, C., Wei, X., Kysar, J. W., and Hone, J., 2008, "Measurement of the Elastic Properties and Intrinsic Strength of Monolayer Graphene," Science, **321**(5887), pp. 385–388.
[47] Hu, Y.-G., Liew, K. M., Wang, Q., He, X. Q., and Yakobson, B. I., 2008, "Nonlocal Shell Model for Elastic Wave Propagation in Single- and Double-Walled Carbon Nanotubes," J. Mech. Phys. Solid., **56**(12), pp. 3475–3485.